Bioinspired Functional Surfaces Enabled by Multiscale Stereolithography

*Yuanrui Li, Huachao Mao, Pan Hu, Mark Hermes, Haneol Lim, Jongseung Yoon, Mitul Luhar, Yong Chen, and Wei Wu**

Additive manufacturing has many advantages in creating highly complex customized structures. In this study, a low-cost multiscale stereolithography technology that can print a macroscale object with microscale surface structures with high throughput is demonstrated. The developed multiscale stereolithography is realized by dynamic switching of laser spot size and adaptively sliced layer thickness. An optical filter based on subwavelength resonance grating is used to modify laser spot size for lasers with different wavelengths and achieves a maximum resolution of 37 μm. The multiscale stereolithography process has 4.4× throughput improvement compared with the traditional stereolithography process with a single laser spot. For proof-of-concept testing, artificial shark skins with microriblet features are designed and 3D printed. In pipe flow experiments, the 3D printed shark skin demonstrates almost 10% average fluid drag reduction. Artificial lotus leaf surfaces are also 3D printed to demonstrate superhydrophobic property. This new process has the potential to serve as a powerful tool that can bring bioinspired structures into real-life applications.

Nature is an exceptional source of inspiration for designing multifunctional surfaces and structures.[1] Many structures in nature can be transferred into technologies that have big economic impact. As an example, the textured skin of fast swimming sharks has been drawing attention for nearly three decades. Shark skin has superficial structures (**Figure 1**a) known as denticles that are thought to be multifunctional. It has been hypothesized that these surface features prevent biofouling and, more importantly, reduce fluid friction drag, which enables more efficient swimming. This has inspired the development of commercially successful products such as the Fastskin swimming suit by Speedo. Shark skin structures could also be applied to ships, underwater vehicles, airplanes, and pipelines to reduce energy waste from friction drag.

Many studies have been conducted over the past few decades to understand the mechanism of drag reduction over shark skin–inspired surfaces. The physical causes responsible for drag reduction are reasonably well understood.[2–4] However, fabrication of such multifunctional surfaces remains a challenge. Although various methods have been used to reproduce shark skin geometry, a trade-off between throughput and resolution always exists and severely hinders the progress in this field. Some high-throughput methods include textured liners,[5,6] molding from real shark skin samples,[7] microcasting and wax printing, sampling from real shark skin,[8] and laser cutting.[9] However, these methods suffer from low resolution or difficulty in accurately reproducing the 3D geometry of shark skin, comprising dermal denticles attached to the surface. More importantly, given the vast design spaces involved, it is difficult to flexibly and quickly fabricate many different modified shapes and sizes that may be required in biomimetic studies. High-resolution digital fabrication methods such as two-photon lithography[10] have successfully fabricated highly detailed and accurate 3D shark skin denticles.[9] However, such fabrication processes can only produce samples with small areas. The small building extent, coupled with extremely low throughput, limits the value of such fabrication techniques for research purposes. As an emerging manufacturing technology, 3D printing has been playing an increasingly important role in various industries due to its advantages in high customization and fast prototyping, as well as the ability to fabricate complex shapes.[11–17] The flexibility of 3D printing also makes it very appealing for biomimetic studies. For example, 3D printing enables the development of artificial shark skin with textures of varying shape and size on arbitrary surface shapes. Indeed, some recent studies have successfully utilized 3D printing to fabricate shark skin structures.[9,18,19] Nevertheless,

Y. Li, P. Hu, Prof. W. Wu
Ming Hsieh Department of Electrical Engineering
University of Southern California
Los Angeles, CA 90089, USA
E-mail: wu.w@usc.edu

H. Mao, Prof. Y. Chen
Daniel J. Epstein Department of Industrial and Systems Engineering
University of Southern California
Los Angeles, CA 90089, USA

M. Hermes, Prof. M. Luhar
Department of Aerospace and Mechanical Engineering
University of Southern California
Los Angeles, CA 90089, USA

H. Lim, Prof. J. Yoon
Mork Family Department of Chemical Engineering and Materials Science
University of Southern California
Los Angeles, CA 90089, USA

The ORCID identification number(s) for the author(s) of this article can be found under https://doi.org/10.1002/admt.201800638.

DOI: 10.1002/admt.201800638

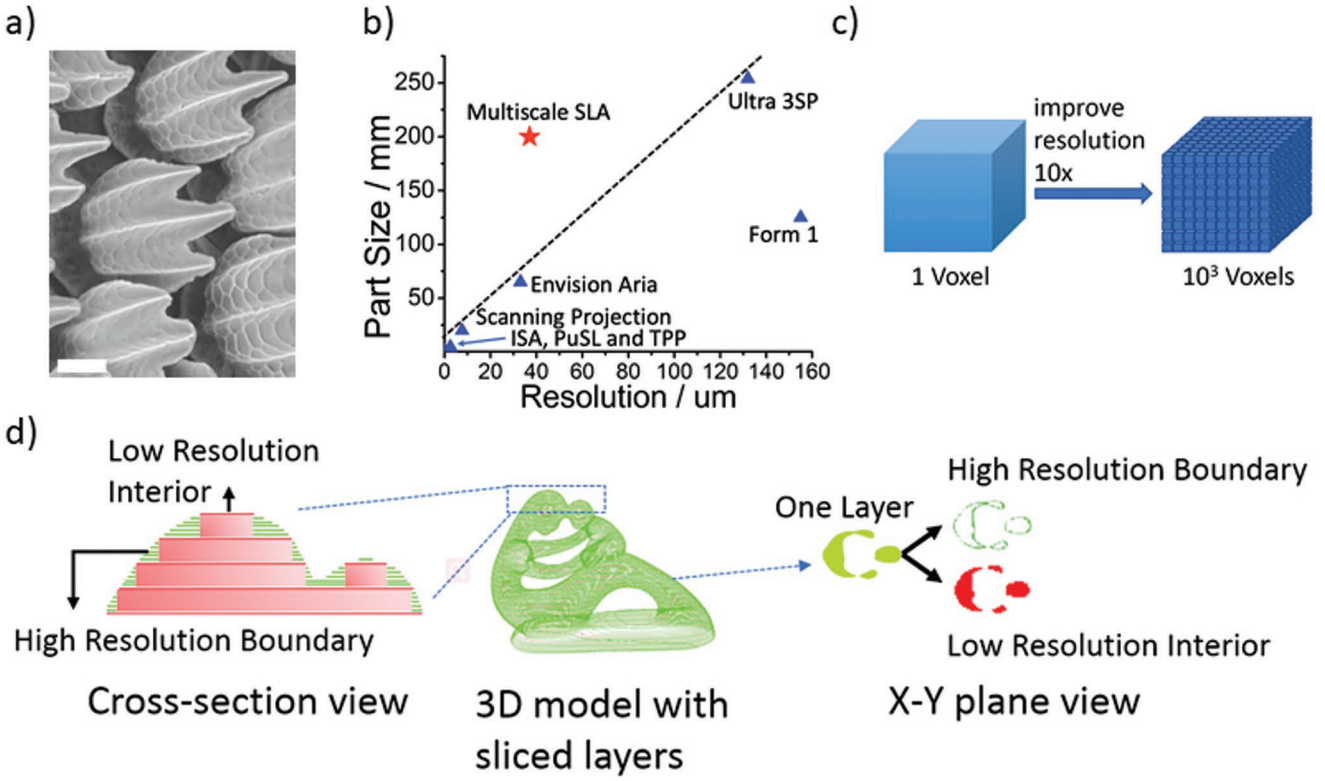

Figure 1. a) SEM image of denticles from a bonnethead shark. Scale bar, 50 µm.[8] b) Relationship between 3D printing resolution and overall part size for several current technologies. Observe that larger the part size is, the worst the feature resolution will be. This is a trade-off between resolution and throughput. Data sourced from commercial products, Formlab Form 1, Envisiontec Ultra 3SP, Envision Aria and publications.[42–46] c) The effect of resolution increases on the total number of voxel required. In this case, printing resolution is improved 10 times. To fill the same amount of volume, we need 10^3 smaller voxels. In general, linear increase of resolution results in a cubic growth of the number of voxel. d) Adaptive layer thickness in a digital model. The sample input is a 3D sculpture with high surface resolution. In the *x*–*y* plane, high- and low-resolution areas are separated and printed with different laser beams. In the *Z* direction, the high-resolution area is sliced into thin layers and the low-resolution area is sliced into thick layers.

the trade-off between throughput and resolution is an important bottleneck that limits the use of 3D printing in multiscale fabrication, as is typically required in biomimetic studies (Figure 1b). As a result, the 3D-printed shark skin denticles employed in previous studies have been scaled up from real sizes.[18,19] These limitations highlight the need for appropriate tools that can fabricate fine features over large surface areas, i.e., create real-scale shark skin features over the large surface areas necessary for hydrodynamic testing. As Figure 1b shows, with current 3D printing technologies, the ratio between part size and resolution is typically around 1000. Hence, current 3D printing technologies must sacrifice resolution when part size grows. This is primarily because the cost to increase throughput while maintaining resolution is high. For instance, the stereolithography process fabricates object with individual voxels, the counterpart of pixels in 3D space. If the size of each voxel is shrunk linearly to increase resolution, the total number of voxels required would grow cubically (Figure 1c). This would increase fabrication time and modeling workload significantly. To print a macroscopic object with microscale shark skin textures, the ratio between part size and resolution can easily exceed 10^4, which we define as a *multiscale* process. Stereolithography machines with a fixed voxel size will not execute multiscale processes well due to the cubic growth of fabrication time and modeling workload.

In this work, we demonstrated a low-cost(built under $2500) multiscale stereolithography technology that can achieve both high resolution and throughput at the same time. Our multiscale stereolithography process consists of two parts: variable beam profile with different spot sizes in the *X*–*Y* plane and adaptive slicing layer thickness in the *Z* direction. To test this multiscale printing process, we fabricated large area samples with sub-50 µm riblet and denticle features. The multiscale printing process involved the following key steps. First, the input digital model was divided into a low-resolution portion and a high-resolution portion. The high-resolution portion (i.e., with denticle structures) was sliced into much thinner layers and printed by a small laser beam; while the low-resolution portion was sliced into thicker layers and printed by a larger laser beam. The benefit of this method can be shown by an example in Figure 1d where the model is a sculpture with high surface resolution. It can be observed that the low-resolution part takes up most of the volume. Using thicker layers and the larger laser beam, this large volume can be fabricated with high throughput. On the other hand, the high-resolution portion requires thinner layers and the smaller laser beam, but does not take much time as it only constitutes a small portion of the object volume.

A schematic of the multiscale stereolithography setup is shown in **Figure 2**a. Two lasers of 405 and 445 nm wavelength,

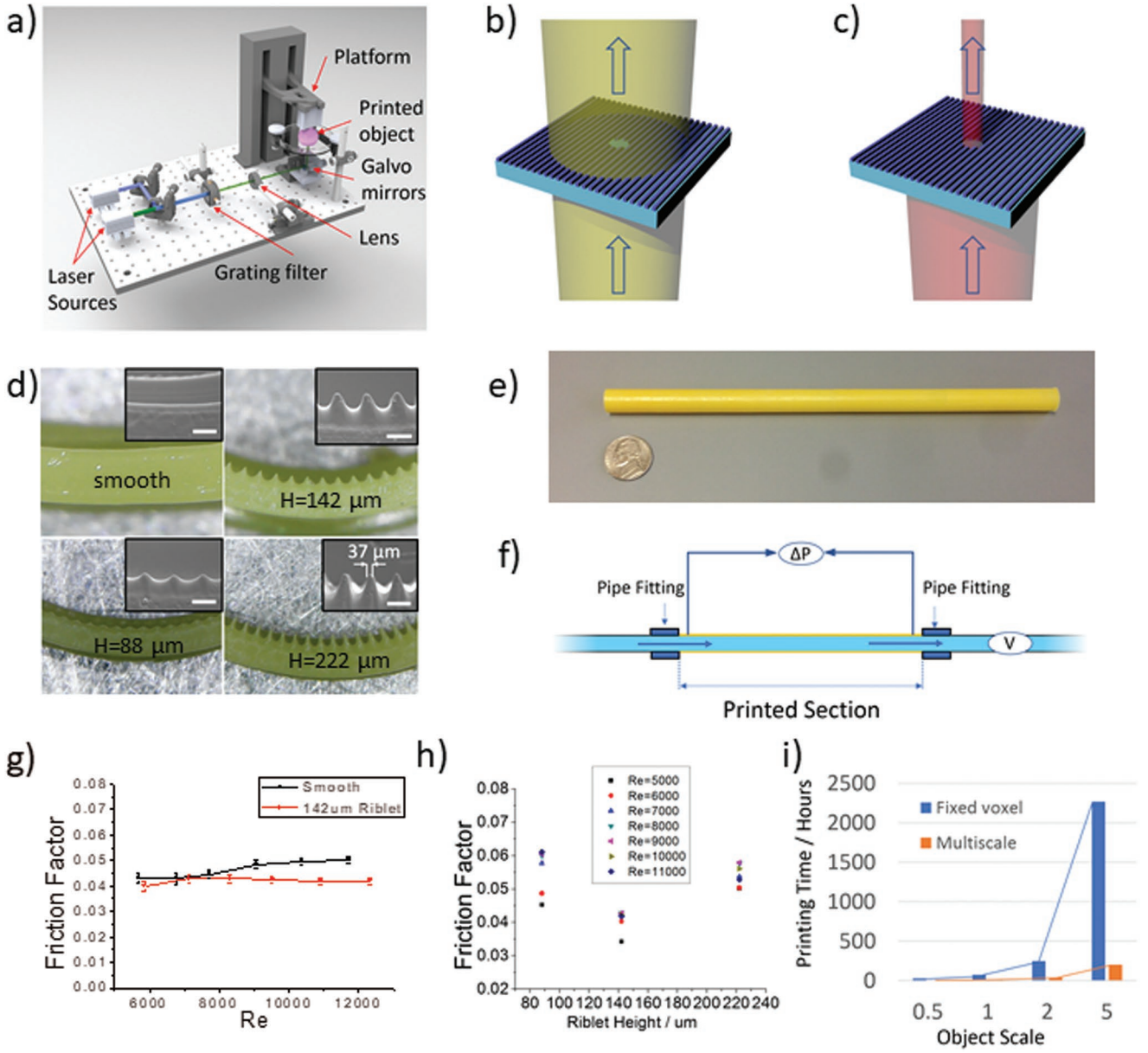

Figure 2. a) 3D diagram of the complete multiscale stereolithography setup. The two lasers have wavelength of 405 and 445 nm, respectively. b,c) Schematics of beam profile switching process with resonance grating filter. The optical filter has different transmission properties for different wavelengths: (b) For $\lambda_1 = 445$ nm the filter is transparent and gives a larger laser spot (≈300 µm) on the resin surface. (c) For $\lambda_2 = 405$ nm, only the central area is transparent. The filter works as an aperture and gives a smaller (≈25 µm) laser spot on the resin surface. d) Cross-section view of four pipes with different interior textures. Scale bar for the SEM images, 200 µm. e) Comparison of the overall size of a printed multiscale pipe with a quarter dollar coin. f) Schematic of pipe flow setup. g) Measured friction factors for the smooth pipe and the pipe with 142 µm riblets. h) Comparison of friction factors of the pipes with different riblet height. i) Printing time of fixed voxel process and variable voxel multiscale process at different object size scale.

respectively, are used, and the two laser beam paths are aligned and combined into the same optical path.[20] During the printing process, only one of the laser beams is turned on. The laser beams go through a specially designed resonance grating filter. The resolution switching comes from two different transmission responses that the filter has for the two wavelengths (Figure 2b,c). The filter is based on subwavelength resonance grating structure.[20] For the 445 nm light, the filter is nearly transparent and produces a 300 µm size laser spot. For the 405 nm wavelength, the grating covered area is highly reflective to this wavelength and only a circular area of 25 µm diameter without gratings is transparent. Therefore, the filter works as an aperture that can dynamically switch laser spot size between 300 and 25 µm for the two laser sources with different wavelengths. After the filter, the laser beam goes through the focusing lens and two galvomirrors and is finally projected onto the resin surface. The galvomirrors change the direction of the laser beam to trace a cross-section of the object being printed. Compared to other variable resolution techniques that involve mechanical motion,[21–23] our method based on a grating filter

has several advantages: 1) The laser spot size is changed by switching wavelengths which can be done in 50 µs or less; this saves manufacturing time as resolution switching frequently happens in every layer. 2) The possibility of misalignment due to mechanical motion is eliminated, which is important for high-resolution printing (<50 µm). 3) The cost of the machine is relatively inexpensive since it shares most of the components with existing stereolithography machines and there is no need for precision motion components. 4) It is possible to stack multiple filters together, and each filter works for a different wavelength. In this case, a library of beam shapes can be realized in a similar fashion to shaped-beam electron-beam lithography.[24]

In terms of the z direction slicing used in the printing process, an adaptive layer thickness method[25,26] was used. The different slicing layers used for printing the pipe and denticle structures in the flow experiments described below are shown in Figure 2d. The large feature portion was sliced into thick layers of 100 µm layer thickness and the small feature portion was sliced into thin layers of 20 µm layer thickness. Combining the beam size switching and adaptive layer thickness, the following strategy was then used to fabricate the sliced layers:

a) Use the small laser spot (25 µm using the laser with 405 nm) to fabricate the small features in the current thin layer.
b) Move the Z linear stage up by a layer thickness of 20 µm.
c) Repeat steps a, b until five thin layers are printed
d) Move the Z stage up for 1 mm and down to allow the resin to flow and coat the entire cross-section.
e) Use the big laser spot (300 µm using the laser with 445 nm) to fabricate the large features in the current thick layer.
f) Repeat steps a–e until the whole object is fabricated.

Compared to stereolithography with fixed voxel size, the time savings generated by our printing process can be attributed to two factors. First, the large laser spot size and thick layer thickness make printing the low-resolution area much faster. Second, since the high-resolution features have a small cross-section area, it is easy for the resin to flow in. This means that the recoating operation is not necessary between each thin layer, and can therefore be removed.

To demonstrate the utility of our multiscale printing process, we conducted hydrodynamic experiments measuring fluid friction in pipes with varying shark skin–inspired textures. Several pipes with different microstructures on their inner walls (Figure 2d) were printed so that they could be tested in a standard pipe flow pressure drop experiment as shown in Figure 2f. Details of the experiment is included in Experimental Section. The length of all four pipes was 18.7 cm and the internal diameter was 9.4 mm. Figure 2e shows the overall size of one of the pipes. One of the pipes had a smooth bore (no microstructure); this was used as the baseline reference. The second pipe had riblets with a height of 142 µm, which proved to be optimal for drag reduction. An additional two pipes with riblet height 88 and 222 µm were also printed to test the effect of texture size on drag reduction. The maximum feature resolution was 37 µm as shown in Figure 2d. It is worth mentioning that higher resolution can be easily realized by using lenses with larger numerical aperture which is not necessary for this work and may increase the setup cost.

Friction factor estimates for the smooth bore pipe and the pipe with the optimal 142 µm riblets are plotted in Figure 2g as a function of the Reynolds number, $Re = \frac{\rho \langle U \rangle D}{\mu}$, in which μ is the dynamic viscosity of water. Note that the Reynolds numbers in the experiment ranged between $Re \approx 5000$ and $Re \approx 12\,000$. Over this entire range of Reynolds number, the pipe with riblets had a smaller friction coefficient compared to the smooth bore pipe, indicating drag reduction. The degree of drag reduction varied with Reynolds number. On average, the friction coefficient was 0.046 ∓ 0.0017 for the smooth pipe and 0.042 ∓ 0.0016 for the pipe with riblets, which yields an average drag reduction of 9.6%. To study how riblet geometry affects drag, both taller and shorter riblets were also tested. The measured friction factors are shown in Figure 2h. The measurements demonstrate that, for the conditions tested, the 142 µm riblets yielded the best performance. Both increasing and reducing the riblet height worsened performance.

The observations described above are in broad agreement with previous results, which demonstrate that riblets can generate as much as 10% drag reduction.[2,27] Further, previous experimental and numerical studies[2,3,27] also demonstrate a clear optimum in riblet size for given flow conditions. However, the exact numbers obtained here must be treated with some caution. This is because the average friction factor observed for the present smooth bore pipe, $f_D = 0.0463$ is higher than that observed in previous smooth pipe experiments. Specifically, the friction factor typically ranges between 0.04 and 0.03 over the range of Reynolds numbers tested.[28] We attribute this to potential roughness effects since the 3D-printing process with a minimum layer thickness of 20 µm yields a rougher surface than that in finely polished or honed pipes. Nevertheless, the current measurements provide a nice demonstration of potential applications.

To demonstrate advantages in the throughput of the multiscale printing process, several pipes with different dimension scales were printed and the printing time was recorded (Figure 2i). At scale 1, the pipe was of 200 mm length, 12 mm diameter, 1.5 mm wall thickness, 237 µm riblet pitch, and 142 µm riblet height. In other words, the scale 1 pipe has dimensions similar to the samples used in pipe flow testing, as shown in Figure 2f. For the other scales, riblet dimensions remained the same while the overall size of the pipe changed in every direction. This test was carried out to simulate the situation in which larger samples are needed for real-world application, but the high-resolution features need to be maintained to ensure surface function. As shown in Figure 2i, at scale 0.5, the multiscale process is about 3.8× faster than the fixed voxel process. The speedup ratio increases to 4.4 at scale 1 and 11 at scale 5. Note that data for scale 2 and 5 were extrapolated from printing time of pipes shorter than required. The results shown in Figure 2i demonstrate that the multiscale process becomes more advantageous as the object scale increases. This can be explained by the equations below

$$t_{\text{fixed}} \propto \frac{L^3}{V_{\text{small voxel}}}$$

$$t_{\text{multi}} \propto \frac{L^3}{V_{\text{big voxel}}} + h \cdot \frac{L^2}{V_{\text{small voxel}}}$$

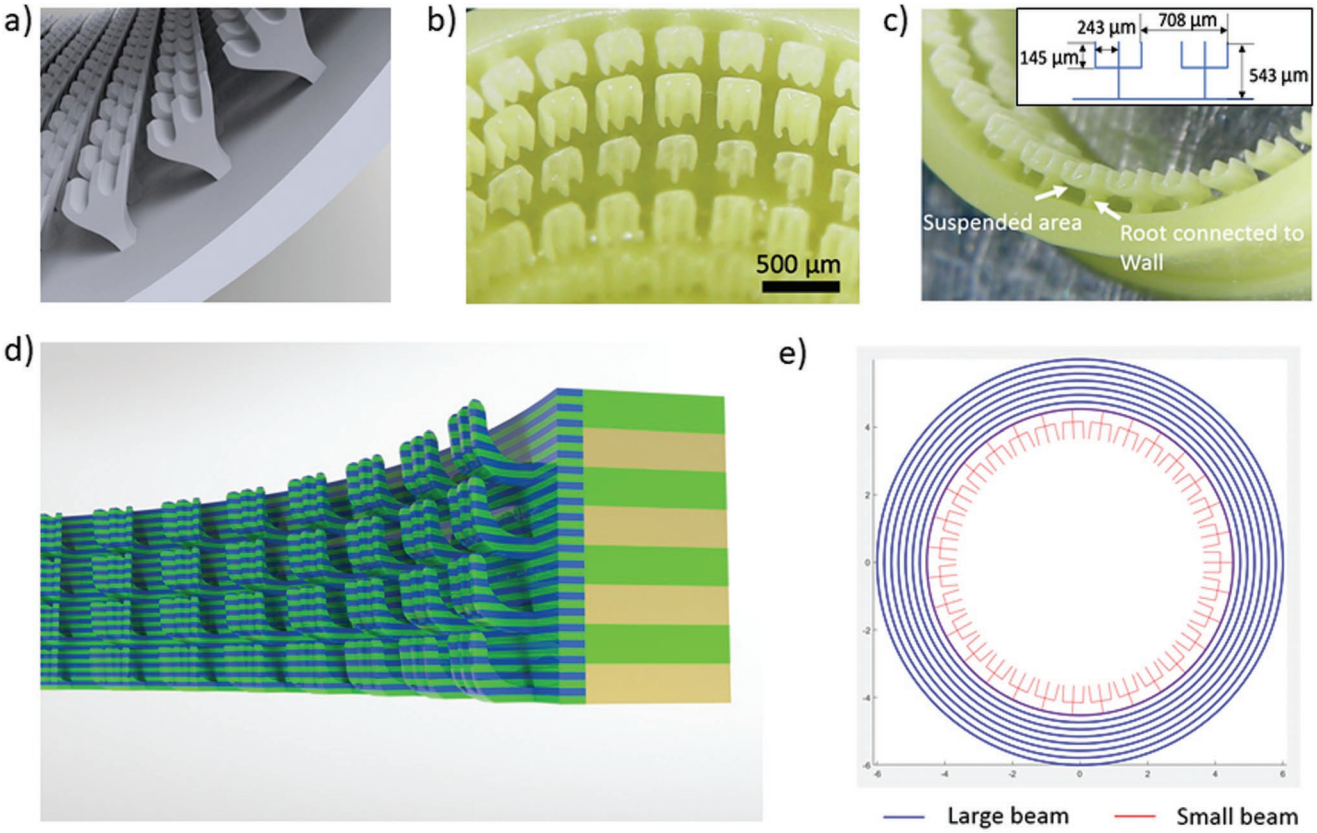

Figure 3. a) 3D model of denticles. b) Printed denticles. c) The cross-section of a sample which shows the suspended area of printed denticles. d,e) Multiscale printing of denticles: (d) adaptive layer thickness. Different colors denote different layers during printing. (e) Cross-section view of a layer showing beam switching within a single layer. For the denticle features in the inner surface, the small laser beam was used for high resolution. For the pipe wall, the large laser beam was used for high throughput.

where L is the object size. The printing time for the fixed voxel process is proportional to object volume divided by voxel volume. Since the voxel volume is a constant, the printing time grows cubically as the object size increase. The printing time for the multiscale process consists of two terms. The first term is the object volume divided by the big voxel size indicating interior structure printing time. The second term is the object surface area divided by small voxel size indicating surface high resolution printing time. The cubic growth in the first term can be compensated by using a cubically larger voxel volume, $V_{\text{big voxel}}$. With this, the time required depends primarily on the high-resolution surface term, which grows quadratically with object scale. This results in potential time savings of order L/h compared to the fixed voxel process.

In addition to the relatively simple (effectively 2D) riblet features, we also fabricated large area complex denticle structures with sub-50 µm feature size. To our knowledge, this has not been demonstrated before. The design is illustrated in **Figure 3**a, which shows a pipe with a denticle covered interior. The actual printed sample is shown in Figure 3b,c. The images clearly show that a big part of each denticle is suspended which is hard to fabricate using manufacturing techniques other than 3D printing technology. Figure 3d,e shows details about how the denticle structure is printed by the multiscale stereolithography process. The designed digital model is first sliced into layers with the adaptive layer thickness. The high-resolution features—the denticles and a thin layer of the wall that they connect to—are sliced into thin layers of 20 µm thickness. The low-resolution feature—the pipe wall—is sliced into thick layers of 100 µm thickness. The printing sequence is the same as previously described. Beam diameter is switched when transitioning from high-resolution to low-resolution features. The denticles were printed with the small laser beam of 25 µm diameter. The pipe wall was printed with the large laser beam of 300 µm diameter.

With the help of multiscale stereolithography process, many other biomimetic structures may be fabricated and studied experimentally. As an example, **Figure 4**b shows an artificial lotus leaf with micropillars which has water repellent function, printed using the same process. A contact angle of 139° was measured on the artificial lotus leaf with 300 µm pillar pitch using a water droplet of 10 µL volume. Although the angle is smaller than that on a lotus leaf in nature(Figure 4a) which can be larger than 150°,[29] it is a preliminary result showing that similar structure can be easily fabricated with the process. Structure optimization and detailed characterization will be included in future works.

In summary, a multiscale stereolithography (SLA) process was developed to address one of the central limitations associated with existing additive manufacturing technologies: the

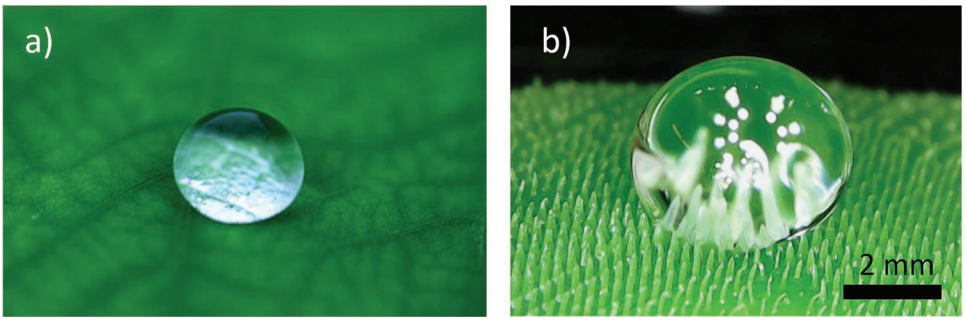

Figure 4. A drop of water on the surface of a) a lotus leaf in nature,[47] b) an artificial lotus leaf printed by the multiscale stereolithography process. The pitch between the micropillars is 300 µm.

trade-off between throughput and resolution. The multiscale stereolithography process consists of two parts. In the *X*–*Y* plane, a resonance grating filter is used to switch the laser beam profile for different laser wavelengths. In the *Z* axis, an object is built by using an adaptive layer thickness for large and small features. The multiscale SLA machine is low cost, miniaturized, and precise. Artificial shark skin samples with riblets and denticles were printed. The riblet with optimum height demonstrated almost 10% average drag reduction. The multiscale SLA process showed 4.3× higher throughput compared to traditional SLA processes. Moreover, this advantage becomes even larger when bigger objects need to be printed. We also fabricated large area samples with denticles that have resolution similar to natural shark skin. These preliminary tests confirm that the present technique yields novel fabrication capabilities that can enable the study and development of multifunctional biomimetic surfaces. Given its ability to simultaneously provide high resolution and throughput using relatively low-cost hardware systems, the multiscale stereolithography process described in this article has the potential to open up many application areas out of reach of current 3D printing technology.

Experimental Section

Fabrication of Laser Beam Profile Switching Filter: The filter consisted of a subwavelength resonance grating[30–35] and a fused silica substrate. This approach was selected because the resulting high reflectivity and small thickness make it possible to stack multiple layers together in order to have more than two beam shapes, similar to shaped-beam electron-beam lithography.[24] The filter started as a fused silica substrate with 400 nm sputter-coated TiO_2. The grating pattern was defined by nanoimprint lithography[36–39] and then followed with reactive ion etching to etch the TiO_2 layer. The grating structure inside a 25 µm diameter circular area at the filter center was removed by photolithography followed by reactive ion etching which created an aperture for 405 nm laser. More details on fabrication can be found in previous publication.[20,40,41]

Characterization: Microstructures on the samples were characterized by scanning electron microscopy (SEM, JOEL JSM-7001) and optical microscope (COLEMETER Handheld Digital Microscope).

Material: The resin used for the printing the shark skin samples was SI 500 from EnvisionTec. The viscosity of the resin was 180 cP at 25 °C. Tensile strength at break was 78 Mpa. Dosage tests were conducted for the 405 and 445 nm laser, respectively, before printing to ensure correct exposure.

Pipe Flow Measurement: The setup is shown in Figure 2f. The test pipe was joined with commercially available smooth pipes. A pair of holes was drilled on the side wall close to the two ends of the test pipe. These holes were connected to a differential pressure transducer that measured the pressure difference between the beginning and the end of the pipe, ΔP, as a function of the flow rate, Q. The pressure drop can be translated to a friction coefficient using the Darcy–Weisbach law: $f_D = \left(\frac{\Delta P}{L}\right)\left(\frac{2D}{\rho\langle U\rangle^2}\right)$, where ΔP is the pressure drop, L is the length of the pipe (187 mm), D is the internal diameter of the pipe, ρ is the density of water, and $\langle U\rangle = 4Q/(\pi D^2)$ is the average flow speed of the water in the pipe cross-section. The pressure drop signal was logged to a computer using a National Instruments Data Acquisition system. The flow rate was measured using a flowmeter at downstream end the of the pipe logged to the computer via an Arduino microcontroller. The water was driven by a commercial water pump in a reservoir. The flow rate was adjusted by a valve at upstream of the test section.

Printing Path Planning Method: A general tool path planning method was developed[25] to dynamically switch laser spot size between 300 and 25 µm, so that the high-resolution features can be preserved by using the small laser spot and the fabrication speed can be largely improved by the large laser spot scanning. The task of tool path planning was generating the scanning paths for the scanner and lasers' ON/OFF status, given a 3D object, formatted as an STL file. As shown in Figure 1d, the 3D model was first sliced into a set of layers with 20 µm layer thickness. For every five layers, their common area is computed and noted as *A*. The interior of this common area was calculated by offsetting *A* inwards with distance *r* (*r* was set as 0.5 mm in all the tests). Notice that this interior was the common interior for all the five layers, and it was filled by scanning the large laser spot, and hence the major area of the part was efficiently solidified. Then, each small layer was only required to fill the boundary region using the small laser spot, and the boundary for each small layer was computed as the whole layer subtracting the common interior. This method can be summarized as:

Algorithm:
Input: a 3D model (STL format)
Output: the tool path (gcode)
Steps:

01: Initialize the output as an empty set $P = \{\}$.
02: Slice the input 3D model into a set of layers using 20 µm layer thickness, noted each layer as L_i.
03: For every five layers
04: Compute the common area of these five layers, denoted as *A*
05: Calculate the interior of *A* by offsetting *A* inwards with distance *r*, noted as $I = A\downarrow r$.
06: For each layer L_j in these five layers
07: Calculate the boundary of each layer as the whole layer subtracting the interior ($L_j - I$).
08: Generate the scanning path for the small laser spot to fill this boundary, and add the path to *P*.
09: End For
10: Generate the scanning path for the large laser spot to fill the common interior *A*, and add this scanning path to set *P*.
11: End For
12: Return the tool path *P*

Acknowledgements

The authors thank the support from The Core Center of Excellence in Nano Imaging (CNI) at USC. W.W. is grateful for the financial support of USC Stevens Center for Innovation Technology Advancement Grant. Y.C. is grateful for the financial support of the National Science Foundation (NSF) (Grant Nos. CMMI-1151191).

Conflict of Interest

The authors declare no conflict of interest.

Keywords

3D printing, biomimetic, functional surfaces, shark skin, stereolithography

Received: November 20, 2018
Revised: December 23, 2018
Published online:

[1] *Functional Surfaces in Biology*, Vol. *1*, Springer, Netherlands **2009**.
[2] R. GarcÍA-Mayoral, J. JimÉNez, *J. Fluid Mech.* **2011**, *678*, 317.
[3] H. Choi, P. Moin, J. Kim, *J. Fluid Mech.* **1993**, *255*, 503.
[4] P. Luchini, F. Manzo, A. Pozzi, *J. Fluid Mech.* **2006**, *228*, 87.
[5] M. T. A. Saif, D. Joseph, O. Riccius, C. Christodoulou, *AIAA J.* **1990**, *28*, 1697.
[6] E. Koury, P. S. Virk, *Appl. Sci. Res.* **1995**, *54*, 323.
[7] G. D. Bixler, B. Bhushan, *Soft Matter* **2012**, *8*, 11271.
[8] J. Oeffner, G. V. Lauder, *J. Exp. Biol.* **2012**, *215*, 785.
[9] G. V. Lauder, D. K. Wainwright, A. G. Domel, J. C. Weaver, L. Wen, K. Bertoldi, *Phys. Rev. Fluids* **2016**, *1*, 060502.
[10] M. Deubel, G. von Freymann, M. Wegener, S. Pereira, K. Busch, C. M. Soukoulis, *Nat. Mater.* **2004**, *3*, 444.
[11] T. M. Barker, W. J. S. Earwaker, D. A. Lisle, *Australas. Radiol.* **1994**, *38*, 106.
[12] S. Nikzad, A. Azari, *J. Oral Maxillofac. Surg.* **2008**, *66*, 1446.
[13] J. Ruppin, A. Popovic, M. Strauss, E. Spuntrup, A. Steiner, C. Stoll, *Clin. Oral Implants Res.* **2008**, *19*, 709.
[14] O. Ozan, I. Turkyilmaz, A. E. Ersoy, E. A. McGlumphy, S. F. Rosenstiel, *J. Oral Maxillofac. Surg.* **2009**, *67*, 394.
[15] J. Giannatsis, V. Dedoussis, D. Karalekas, *Rapid Prototyping J.* **2002**, *8*, 200.
[16] Y. Yang, X. Li, X. Zheng, Z. Chen, Q. Zhou, Y. Chen, *Adv. Mater.* **2018**, *30*, 1704912.
[17] Y. Yang, X. Song, X. Li, Z. Chen, C. Zhou, Q. Zhou, Y. Chen, *Adv. Mater.* **2018**, *30*, 1706539.
[18] L. Wen, J. C. Weaver, G. V. Lauder, *J. Exp. Biol.* **2014**, *217*, 1656.
[19] L. Wen, J. C. Weaver, P. J. Thornycroft, G. V. Lauder, *Bioinspiration Biomimetics* **2015**, *10*, 066010.
[20] Y. Li, H. Mao, H. Liu, Y. Yao, Y. Wang, B. Song, Y. Chen, W. Wu, *J. Vac. Sci. Technol., B: Nanotechnol. Microelectron.: Mater., Process., Meas., Phenom.* **2015**, *33*, 06F604.
[21] D. Miller, C. Deckard, J. Williams, *Rapid Prototyping J.* **1997**, *3*, 4.
[22] J.-H. Sim, E.-D. Lee, H.-J. Kweon, *Int. J. Precis. Eng. Manuf.* **2007**, *8*, 50.
[23] C. Yi, L. Dichen, W. Jing, *Rapid Prototyping J.* **2013**, *19*, 100.
[24] Y. Nakayama, S. Okazaki, N. Saitou, H. Wakabayashi, *J. Vac. Sci. Technol., B: Microelectron. Nanometer Struct.* **1990**, *8*, 1836.
[25] H. Mao, Y.-S. Leung, Y. Li, P. Hu, W. Wu, Y. Chen, **2017**, *2*, V002T01A033.
[26] H. Mao, T.-H. Kwok, Y. Chen, C. C. L. Wang, *Comput.-Aided Des.* **2019**, *107*, 89.
[27] D. W. Bechert, M. Bruse, W. Hage, J. G. T. van der Hoeven, G. Hoppe, *J. Fluid Mech.* **1997**, *338*, 59.
[28] L. F. Moody, *Trans. ASME* **1944**, *66*, 671.
[29] T. Darmanin, F. Guittard, *Mater. Today* **2015**, *18*, 273.
[30] Y. Yao, H. Liu, Y. Wang, Y. Li, B. Song, R. P. Wang, M. L. Povinelli, W. Wu, *Opt. Express* **2016**, *24*, 15362.
[31] Y. Yao, H. Liu, W. Wu, *Appl. Phys. A* **2014**, *115*, 713.
[32] Y. Yao, H. Liu, W. Wu, *J. Vis. Exp.* **2015**, *101*, e52913.
[33] Y. Yao, H. Liu, W. Wu, *J. Vac. Sci. Technol., B: Nanotechnol. Microelectron.: Mater., Process., Meas., Phenom.* **2014**, *32*, 06FG04.
[34] Y. Yao, Y. Wang, Y. Li, H. Liu, B. Song, W. Wu, presented at *SPIE OPTO*, San Francisco, CA, February **2017**.
[35] Y. Yao, W. Wu, *Adv. Opt. Mater.* **2017**, *5*, 1700090.
[36] B. Song, Y. Yao, R. E. Groenewald, Y. Wang, H. Liu, Y. Wang, Y. Li, F. Liu, S. B. Cronin, A. M. Schwartzberg, S. Cabrini, S. Haas, W. Wu, *ACS Nano* **2017**, *11*, 5836.
[37] Y. Yao, H. Liu, Y. Wang, Y. Li, B. Song, A. Bratkovsk, S.-Y. Wang, W. Wu, *Appl. Phys. A* **2015**, *121*, 327.
[38] J.-B. Wu, H. Zhao, Y. Li, D. Ohlberg, W. Shi, W. Wu, H. Wang, P.-H. Tan, *Adv. Opt. Mater.* **2016**, *4*, 756.
[39] C. Larson, Y. Li, W. Wu, H. Reisler, C. Wittig, *J. Phys. Chem. A* **2017**, *121*, 4968.
[40] H. Liu, Y. Yao, Y. Wang, W. Wu, *J. Vac. Sci. Technol., B* **2014**, *32*.
[41] Y. Yao, Y. Wang, H. Liu, Y. Li, B. Song, W. Wu, *Appl. Phys. A* **2015**, *121*, 399.
[42] J.-F. Xing, X.-Z. Dong, W.-Q. Chen, X.-M. Duan, N. Takeyasu, T. Tanaka, S. Kawata, *Appl. Phys. Lett.* **2007**, *90*, 131106.
[43] J. R. Tumbleston, D. Shirvanyants, N. Ermoshkin, R. Januszieiwicz, A. R. Johnson, D. Kelly, K. Chen, R. Pinschmidt, J. P. Rolland, A. Ermoshkin, E. T. Samulski, J. M. DeSimone, *Science* **2015**, *347*, 1349.
[44] X. Li, Y. Chen, *J. Manuf. Processes* **2017**, *28*, 531.
[45] M. P. Lee, G. J. Cooper, T. Hinkley, G. M. Gibson, M. J. Padgett, L. Cronin, *Sci. Rep.* **2015**, *5*, 9875.
[46] C. Sun, N. Fang, D. M. Wu, X. Zhang, *Sens. Actuators, A* **2005**, *121*, 113.
[47] Lotus effect, http://www.hk-phy.org/atomic_world/lotus/lotus01_e.html (accessed: May 2018).

